Hot surface ignition of a wall-impinging fuel spray: Modeling and analysis using large-eddy simulation

Danyal Mohaddes [a],*, Philipp Boettcher [b], Matthias Ihme [a]

[a] *Department of Mechanical Engineering, Stanford University, California 94305, USA*
[b] *Boeing Research & Technology, Golden, CO 80403, USA*

ARTICLE INFO

ABSTRACT

The accidental ignition of liquid fuels is an industrial safety concern due to the storage and transport of pressurized flammable liquids near components at elevated temperatures. In this work, a liquid *n*-dodecane fuel spray is considered that impinges on a hot surface, undergoing thermal ignition. Surface temperatures above the minimum hot surface ignition temperature (MHSIT) for *n*-dodecane ignition at atmospheric pressure are considered. At these temperatures, the interaction of the spray with the hot surface is governed by the Leidenfrost effect, resulting in inelastic reflection of impinging droplets. Large-eddy simulations are employed with finite-rate chemistry using a realistic 54-species chemical mechanism with low-temperature ignition chemistry. An Eulerian-Lagrangian approach is taken to the describe the spray dynamics. Ignition kernel formation and propagation are discussed in physical and composition spaces, and the flow field structure is compared to theory. At temperatures near the MHSIT, the secondary flow resulting from the spray impingement in the form of a toroidal vortex is shown to enhance scalar mixing. Low-temperature ignition within the vortex is seen to significantly precede high-temperature ignition near the wall and subsequent rapid flame propagation. At higher wall temperatures, the ignition delay is greatly reduced such that high temperature ignition occurs prior to the establishment of mixing structures, and hence the extent of flame propagation is diminished, with transition occurring rapidly to a steady-burning regime. This study provides fundamental understanding of the physical phenomena involved in the thermal ignition of impinging sprays in different temperature regimes toward the goal of improved industrial safety.

1. Introduction

Accidental ignition is a critical safety concern for many industries. In particular, the ignition of fuel sprays by hot surfaces is a hazard that is present in a wide range of industries and consumer applications that operate with flammable liquids. These include the automotive, aerospace, chemical, and petroleum industries. In these industries, a variety of pressurized flammable liquids are transported next to components at elevated temperatures, where a leak would create the potential for ignition of the liquid spray by the hot surface. Such a leak may result in the formation of an evaporating fuel film on the hot surface or the splashing and rebound of the impinging spray due to the Leidenfrost effect. With the exception of the ambient pressures involved, this problem is similar to that found in direct-injection internal combustion engines, where the injected fuel spray can impinge on the hot

cylinder wall and piston, form an evaporating fuel film and result in exacerbation of emissions, particularly during cold start. In gas turbine engines and liquid rocket engines, the fuel spray may impinge on the combustor walls during operation, where in the latter case it may be used as a design feature to promote combustor wall cooling.

Ignition by hot surfaces has been studied for both gaseous and liquid fuels in both premixed and non-premixed regimes. Early theoretical work by Law [1] and Laurendeau [2] established the importance of surface temperature, pressure and flow velocity in the premixed context. Experimental and numerical studies of premixed hot surface ignition by Boettcher et al. [3] and Boeck et al. [4] demonstrated the tight coupling of transient ignition phenomena with buoyancy-driven flow field dynamics. The interaction of a premixed flame with a liquid fuel film was studied numerically by Desoutter et al. [5] and later by Tao et al. [6] in one-dimensional configurations. These studies showed that the presence of a wall film results in a chemical quenching due to the highly fuel-rich region near the film, as opposed to the thermal quenching typical of

---

* Corresponding author.
  E-mail address: danmohad@stanford.edu (D. Mohaddes).

Table 1

Thermodynamic, physical and other properties of pure and multicomponent heavy hydrocarbon fuels. In this work, n-dodecane is used in the ignition simulations and diesel is used in the evaluation of the spray-wall interaction model. For diesel fuel, T_{sat} refers to the 90% volumetric distillation temperature using ASTM D86. T_{AI} values are based on ASTM E659, which employs air at atmospheric pressure. Physical properties are presented at 1 atm and 400 K for n-dodecane and at 1 atm and 298 K for diesel.

Fuel	T_{sat} [K]	T_L [K]	T_{AI} [K]	ρ_l [kg/m^3]	μ_l [mPa · s]	σ [mN/m]
n-dodecane	489 [57]	558 [58]	476 [59]	669 [57]	0.395 [57]	16 [57]
Diesel	561 [60]	713 [61]	530 [9]	817 [28]	0.316 [28]	28 [28]

a dry wall configuration. Recently, Kats and Greenberg [7,8] have developed a quasi-one-dimensional and static theoretical framework for analyzing the ignition of an impinging fuel spray on a hot surface. They present an ignition criterion based on their asymptotic analysis, which shows a strong dependence on the injected liquid vaporization rate.

Due to its industrial relevance, there have been numerous experimental efforts to characterize the thermal ignition of liquid fuels. Colwell and Reza [9] experimentally studied the minimum hot surface ignition temperature (MHSIT), referred to in this study as T_{HSI}, of automotive and aerospace fuels for single droplets impinging on a hot surface. This study was extended by Davis et al. [10] to consider impinging fuel sprays. Both investigations noted that droplet ignition was a probabilistic and not a threshold phenomenon. Using an impinging spray, T_{HSI} of a number of common aircraft fluids was measured by Johnson et al. [11] in a representative test section of a military aircraft. The authors identified the importance of the Leidenfrost effect on their results, due to its inhibition of direct liquid-solid contact and heat transfer. The thermal ignition of diesel fuel weakly impinging and thus pooling on a hot surface was analyzed by Li et al. [12]. These authors also experimentally identified the Leidenfrost effect as a key physical mechanism in determining ignition behavior. Large-scale experiments performed by Ulcay et al. [13] tested ignition of liquid fuel leaks upstream of hot surfaces in a cross flow. Results showed a dependence of T_{HSI} on the cross-stream air velocity. At temperatures above T_{HSI}, the sensitivity of ignition delay time to wall temperature and system pressure was studied by Chen et al. [14] for an impinging spray of a diesel fuel surrogate. This study showed that ignition kernels are formed near the point of spray impingement and subsequently spread along the wall, and that kernel locations depend on the wall temperature.

An important distinction is made in the literature between the minimum autoignition temperature, T_{AI}, of liquid fuels and the minimum hot surface ignition temperature, T_{HSI}. Determined by standardized experiments, e.g. ASTM E659, T_{AI} represents the lowest temperature for which autoignition is possible given idealized conditions, including residence times of up to ten minutes. Table 1 provides T_{AI} for n-dodecane and diesel fuels. These idealized conditions are typically not representative of hot surface ignition, which is a highly geometry-dependent and probabilistic phenomenon, and may underpredict T_{HSI} for hydrocarbon fuels by up to 400 K [9,10]. Considering a 50 % probability of ignition for wall-impinging fuel sprays at atmospheric pressure, Davis et al. [10] regressed their experimentally-obtained values of T_{HSI} against T_{AI} for a number of hydrocarbon fuels up to n-decane and obtained reasonable agreement. Extrapolating to n-dodecane yields $T_{HSI} \approx 950$ K. In the present study using n-dodecane fuel, the surface temperatures considered are greater than T_{HSI} to ensure ignition.

The interaction of impinging sprays with solid surfaces has been the subject of extensive experimental and numerical investigations [15–20]. At surface temperatures below the saturation temperature T_{sat} of the impinging liquid, depending upon the surface temperature and the kinetic energy of the impinging droplet at impact, the interaction may result in droplet rebound, adherence to the wall, or a combination thereof due to droplet break-up [21]. For

sufficiently high wall temperatures T_w, droplets cannot make direct contact with the solid surface due to the formation of a thin vapor film between the droplet and the solid, known as the Leidenfrost effect [22]. In this regime, all impinging droplets undergo inelastic reflection, potentially with break-up, with the coefficient of restitution being determined solely by the impact energy and not by the surface temperature [23]. For droplets with negligible impact energy, the boundary of the Leidenfrost regime is determined by the Leidenfrost temperature T_L, below which liquid-solid contact may occur. For non-negligible impact energies, a dynamic correction is introduced to obtain the so-called 'dynamic' Leidenfrost temperature $T_{L,dyn} > T_L$ [24]. In the present study, the droplet impact energy is sufficiently low and the surface temperatures considered sufficiently high such that $T_w > T_{L,dyn}$. Table 1 provides values of T_{sat} and T_L for n-dodecane and diesel fuels, where for diesel fuel T_{sat} refers to the 90% volumetric distillation temperature.

The hot surface ignition of premixed gases has been studied both experimentally and numerically, as has been to a lesser extent that of wall-impinging fuel sprays at high ambient pressures where $T_w < T_L$. The behavior of inert sprays impinging on surfaces where $T_w > T_L$ has been analyzed extensively. However, the hot surface ignition of a wall-impinging fuel spray at atmospheric ambient pressure where $T_w > T_L$ remains to be studied. In this regime, a detailed understanding of the coupled physical processes of spray impingement and gaseous mixing and their relationship with low and high temperature ignition chemistry does not yet exist, particularly with regard to the effect of T_w.

The present study seeks to model and analyze the hot surface ignition behavior of an impinging n-dodecane fuel spray at atmospheric pressure using a well-resolved large-eddy simulation (LES). A finite-rate chemistry model including low-temperature ignition chemistry is employed in conjunction with an Eulerian-Lagrangian representation of the gas and liquid phases with a spray-wall interaction model to account for the Leidenfrost effect. The effects of varying T_w on the structure of the ensuing mixing and ignition phenomena are considered.

The remainder of the manuscript is organized as follows. The governing equations for gas and liquid phases, as well as those for spray-wall interactions, are presented in Section 2. The problem configuration is described in Section 3 and is analyzed in the context of the relevant physical phenomena. Details of the computational setup are also given. The gas-phase fluid dynamical structure of the wall-impinging flow is analyzed from a theoretical standpoint in Section 4. Experimental data is used to evaluate the spray-wall interaction model employed in this study in Section 5. Spatially resolved and volume-averaged results of the simulations are presented in Section 6 and are discussed in both physical and composition spaces. The manuscript closes with conclusions in Section 7.

2. Mathematical formulation

2.1. Gas phase equations

In this work an Eulerian-Lagrangian method is employed to describe the coupling between the liquid spray and the gaseous flow

field. The gas phase is modeled as an ideal gas, and is described by the solution of the Favre-filtered compressible Navier-Stokes equations in conservation form augmented with source terms arising from the coupling with the liquid phase

$$\partial_t \bar{\rho} + \nabla \cdot (\bar{\rho}\tilde{\boldsymbol{u}}) = \bar{\dot{S}}_\rho \tag{1a}$$

$$\partial_t (\bar{\rho}\tilde{\boldsymbol{u}}) + \nabla \cdot (\bar{\rho}\tilde{\boldsymbol{u}}\tilde{\boldsymbol{u}}) = -\nabla \bar{p} + \nabla \cdot \bar{\boldsymbol{\tau}}_{\nu+t} + \bar{\dot{\boldsymbol{S}}}_{\rho\boldsymbol{u}} \tag{1b}$$

$$\partial_t (\bar{\rho}\tilde{e}_t) + \nabla \cdot (\bar{\rho}\tilde{\boldsymbol{u}}\tilde{e}_t) = -\nabla \cdot (\bar{p}\tilde{\boldsymbol{u}}) + \nabla \cdot (\bar{\boldsymbol{\tau}}_{\nu+t} \cdot \tilde{\boldsymbol{u}}) - \nabla \cdot \bar{\boldsymbol{q}}_{\nu+t} + \bar{\dot{S}}_{\rho e_t} \tag{1c}$$

$$\partial_t \left(\bar{\rho}\tilde{Y}_k \right) + \nabla \cdot \left(\bar{\rho}\tilde{\boldsymbol{u}}\tilde{Y}_k \right) = -\nabla \cdot \bar{\boldsymbol{j}}_{k,\nu+t} + \bar{\dot{\omega}}_k + \bar{\dot{S}}_{\rho Y_k} \tag{1d}$$

where ρ is the density, $\boldsymbol{u}$ is the velocity vector, p is the pressure, $\boldsymbol{\tau}$ is the viscous stress tensor, e_t is the specific total energy, $\boldsymbol{q}$ is the heat flux, Y_k is the species mass fraction, $\boldsymbol{j}_k$ is the species flux, and $\dot{\omega}_k$ is the species source term. Overbars and tildes denote Reynolds and Favre filtering, respectively. Subscripts ν and t denote viscous and turbulent contributions, respectively, and the subscript k denotes the k-th species. Coupling from the liquid phase to the gas phase is achieved through the inter-phase exchange terms $\dot{S}$.

2.2. Lagrangian spray particle approach

The liquid phase is modeled using a Lagrangian spray-particle (LSP) approach, with the temporal evolution of each droplet governed by [25]

$$d_t \boldsymbol{x}_d = \boldsymbol{u}_d \tag{2a}$$

$$d_t \boldsymbol{u}_d = \frac{f_1}{\tau_d} (\tilde{\boldsymbol{u}}(\boldsymbol{x}_d) - \boldsymbol{u}_d) \tag{2b}$$

$$d_t T_d = \frac{\mathrm{Nu}}{3\mathrm{Pr}_g} \frac{c_p}{c_l} \frac{f_2}{\tau_d} \left(\tilde{T}(\boldsymbol{x}_d) - T_d \right) + \frac{L_\nu}{c_l} \frac{\dot{m}_d}{m_d} \tag{2c}$$

$$d_t m_d \equiv \dot{m}_d = -\frac{\mathrm{Sh}}{3\mathrm{Sc}_g} \frac{m_d}{\tau_d} H_M \tag{2d}$$

where $\boldsymbol{x}_d$, $\boldsymbol{u}_d$, T_d, m_d and $\dot{m}_d$ are the droplet position, velocity, temperature, mass and mass evaporation rate, respectively, and $\tau_d \equiv \rho_l D_d^2/(18\mu)$ is the droplet relaxation time, where ρ_l and D_d are the droplet density and diameter, respectively, and μ is the gas dynamic viscosity. Coupling from the liquid phase to the gas phase is obtained through $\tilde{T}(\boldsymbol{x}_d)$ and $\tilde{\boldsymbol{u}}(\boldsymbol{x}_d)$, which denote the gas-phase temperature and velocity evaluated at the droplet position. Pr_g and Sc_g are the gas-phase Prandtl and Schmidt numbers, respectively, c_p is the gas-phase heat capacity, and c_l and L_ν are the liquid heat capacity and heat of vaporization. The coefficients Nu and Sh are the droplet Nusselt and Sherwood numbers [26], and f_1 is the Stokes drag correction [25]. A non-equilibrium Langmuir-Knudsen model (model M7 in [25]) is used to close the evaporative heat transfer correction f_2 and mass transfer potential H_M.

2.3. Spray-wall interaction modeling

As was discussed in Section 1, when $T_w > T_L$ such that the dynamic Leidenfrost effect prevents liquid film formation, spray-wall interactions with low impact energy result in the inelastic reflection of droplets. In this regime, the change in droplet mass [27] as well as temperature and wall-parallel momentum [23] are negligible during the interaction. The change in wall-normal momentum

has been shown to be significant and well-described by the impact Weber number We_n [23,28]

$$\mathrm{We}_n = \frac{\rho_l u_{d,n}^2 D_d}{\sigma}, \tag{3}$$

where $u_{d,n} = \boldsymbol{u}_d \cdot \hat{\boldsymbol{n}}$ is the droplet wall-normal velocity at impact and $\hat{\boldsymbol{n}}$ is the wall unit normal vector. In the context of the LSP approach, the droplet mass, temperature, and wall-parallel momentum are thus taken as constant during the interaction, and wall-normal momentum loss L_n is modeled using the semi-empirical correlation [23]

$$L_n = \frac{mu_{d,n} - m'u'_{d,n}}{mu_{d,n}} = 0.263\mathrm{We}_n^{0.257} \tag{4}$$

where the prime notation indicates the post-interaction state, and $m = m'$. Droplet deformation effects during spray-wall interaction are thus assumed to be limited to the loss of wall-normal momentum in the present point-particle approximation. Changes to wall temperature due to interaction with droplets in the dynamic Leidenfrost regime have been shown empirically to be small due to the shortness of droplet-wall residence times in this regime [29], on the order of $D_{d,0}/V_d$ [28] and are therefore neglected.

2.4. Finite rate chemistry

The chemical source term in Eq. (1d) is computed using finite rate chemistry. A 54-species reduced chemical mechanism for *n*-dodecane/air combustion is employed [30], with 21 quasi-steady-state (QSS) species identified from the original skeletal mechanism [31] using a level of importance criterion. As shown in Fig. 1a, this mechanism accounts for both low and high-temperature chemistry, with low-temperature chemistry modeled following the work of Bikas and Peters [32]. Further discussion of the present chemical mechanism and its modeling of low-temperature chemistry is available in [33] and [34], respectively.

2.5. Numerical methods

The governing equations Eqs. (1), (2) for the gas and liquid phases are solved using an unstructured, fully compressible finite-volume LES solver. The solver has been validated in a variety of configurations employing finite-rate chemistry and high-fidelity chemical mechanisms, including steady [33] and autoigniting [35] turbulent gas flames, as well as turbulent spray flames [34]. Viscous fluxes are discretized using a nominally 4th-order scheme and a sensor-based hybrid spatial discretization scheme is used for the Euler fluxes, as discussed in Ma et al. [36]. A second-order operator-splitting algorithm that employs a semi-implicit Rosenbrock-Krylov scheme for the temporal integration of the chemistry [37] is augmented for spray combustion simulations by consistently incorporating LSP updates and inter-phase exchanges to ensure global conservation. A second-order implicit scheme is used for the temporal integration of the Lagrangian equations for the spray phase.

2.6. Subgrid-scale modeling

The Vreman model [38] is used for modeling subgrid-scale turbulence in Eq. (1). It is noted that the magnitudes of the subgrid-scale diffusivities in the simulations were found to be small relative to the molecular diffusivities, indicating that the simulation is well-resolved to describe mass, momentum and energy transfer in the gas phase. The dynamic thickened-flame model [39] is used to close turbulence-chemistry interactions with a maximum thickening factor of 5. Consistency between the spray-phase LSP and the gas-phase thickened-flame LES approaches was maintained using the localized re-scaling procedure as in Mohaddes et al. [34].
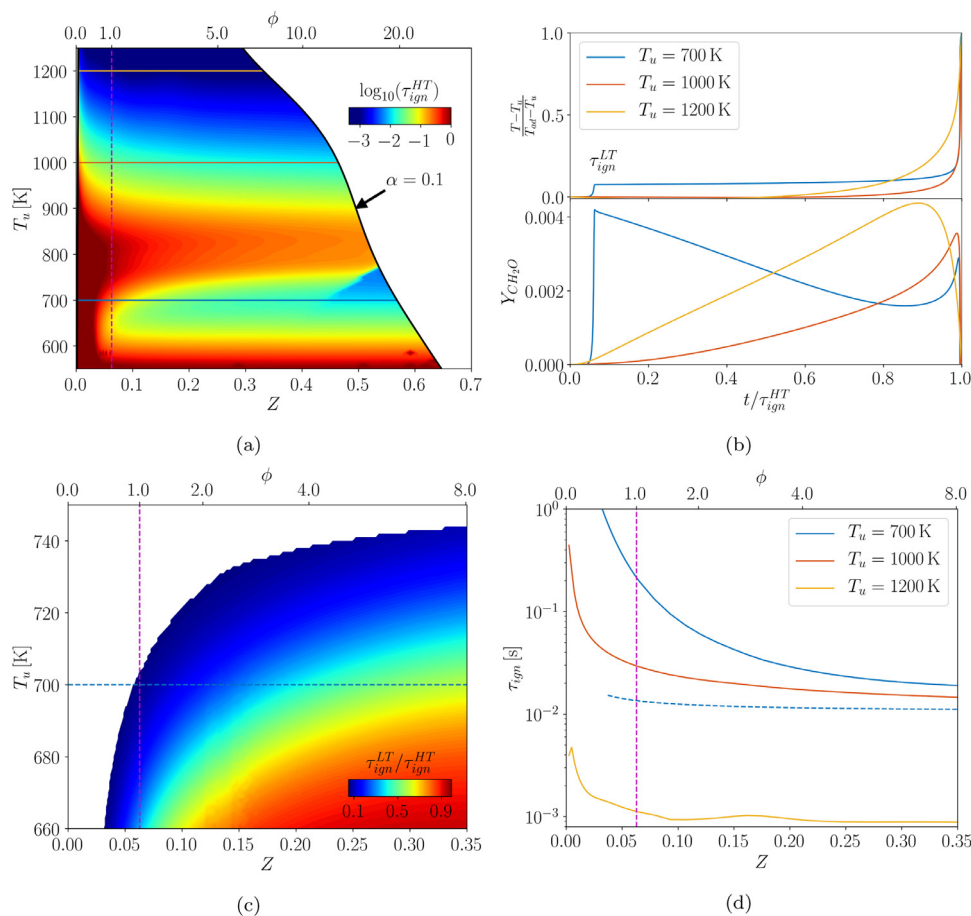
Fig. 1. Homogeneous isobaric adiabatic reactor ignition data obtained at a pressure of 1 atm. (a) High-temperature ignition delay time τ_{ign}^{HT} as a function of Bilger mixture fraction Z and unburned gas temperature T_u. The dashed magenta line indicates the stoichiometric mixture fraction $Z_{st} = 0.0628$, and the upper axis shows the fuel-air equivalence ratio ϕ. The blanked region on the right of the figure corresponds to $\alpha < 0.1$. (b) Temporal evolution of ignition of stoichiometric mixtures exhibiting one and two-stage ignition, with time normalized by τ_{ign}^{HT} for each mixture. (c) Ratio of low-temperature ignition delay time τ_{ign}^{LT} to τ_{ign}^{HT} as a function of Z and T_u. Conditions for which τ_{ign}^{LT} is not defined are blanked. (d) Ignition delay times at multiple unburned gas temperatures as a function of Z. The dashed blue line indicates τ_{ign}^{LT} for mixture fractions at which it is defined at $T_u = 700$ K, and solid lines indicate τ_{ign}^{HT}. At the higher temperatures considered, τ_{ign}^{LT} is not defined. (For interpretation of the references to color in this figure legend, the reader is referred to the web version of this article.)

3. Physical configuration and computational setup

3.1. Motivation for T_w parameter study

In this section, we demonstrate the complexity of the expected thermo-chemical behavior of an igniting wall-impinging spray and its sensitivity to temperature boundary conditions as motivation for studying T_w parametrically. We consider here the ignition delay time of a homogeneous isobaric adiabatic reactor as an idealized low-dimensional model configuration. Figure 1 shows results obtained from homogeneous adiabatic reactor simulations using Cantera [40] at a constant pressure of 1 atm using the reduced chemical mechanism for n-dodecane/air combustion discussed in Section 2.4. We identify low and high-temperature ignition delay times by considering the time required to reach the maximum or maxima in the temporal rate of change of reactor temperature, where the number of such maxima (one or two) indicates whether the ignition was single-stage or two-stage.

We consider first the high-temperature ignition delay time τ_{ign}^{HT} of n-dodecane/air mixtures as a function of initial temperature T_u and initial composition, parametrized by the Bilger mixture fraction Z [41], in Fig. 1a. The figure shows the strong non-monotonicity of τ_{ign}^{HT} with increasing temperature in the range $600 \, \text{K} \lesssim T_u \lesssim 800 \, \text{K}$, referred to as the negative temperature coeffi-

cient (NTC) regime, which is a result of the low-temperature chemistry (LTC) submechanism. Regions where the heat release parameter $\alpha = (T_{ad} - T_u)/T_{ad} < 0.1$, where T_{ad} is the adiabatic flame temperature at a given T_u, have been blanked, as there the reactor is nearly isothermal or indeed endothermic. This occurs for excessively fuel-rich and fuel-lean mixtures. We note that the stoichiometric mixture fraction for n-dodecane/air combustion is $Z_{st} = 0.0628$.

Within the NTC regime, there exists a two-stage ignition regime, with low-temperature ignition occurring at τ_{ign}^{LT}, followed by high-temperature ignition at τ_{ign}^{HT}. In the present nomenclature, τ_{ign}^{HT} is defined for all mixtures where $\alpha > 0.1$, whereas τ_{ign}^{LT} is only defined for mixtures exhibiting two-stage ignition. Figure 1b shows the ignition delay for three temperatures, one of which is in the two-stage ignition regime. The temperature histories for the three stoichiometric mixtures having T_u of 700 K, 1000 K and 1200 K are normalized using their respective adiabatic flame temperatures T_{ad} of 2463 K, 2588 K and 2667 K. The low-temperature ignition delay τ_{ign}^{LT} is clearly visible in the upper panel showing normalized reactor temperature. The lower panel demonstrates a key aspect of LTC, namely the production of formaldehyde. In a two-stage ignition, the low-temperature ignition results in a sharp increase in formaldehyde mass fraction Y_{CH_2O}, which remains high during the inter-stage period, and is then fully consumed during the high-
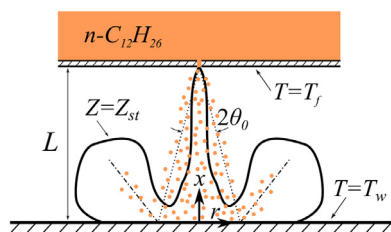
Fig. 2. Schematic representation of the impinging spray configuration prior to ignition. The spray issues from the top of the domain along a nominal ballistic trajectory shown by the dotted lines and impinges on the surface at the bottom of the domain. The dash-dotted lines show the nominal rebound trajectory due to the Leidenfrost effect. The solid line denotes the stoichiometric mixture fraction isocontour, showing the toroidal vortex and the jet-like core.

Table 2
Domain properties and boundary conditions used for the ignition simulations of this study.

Case	T_w [K]	Geometry
TW1000F	1000	Full
TW1000Q	1000	Quarter
TW1200Q	1200	Quarter

temperature ignition. This is in contrast to a single-stage high-temperature ignition, where Y_{CH_2O} increases immediately prior to ignition and is subsequently fully consumed. It is important to note therefore that the mere presence of Y_{CH_2O} is not necessarily indicative of LTC, and must be placed in the context of the local temperature and composition, as is done in this study. Although more direct indicator species for LTC exist, such as the fuel-species-specific alkyl-peroxy radical [42], the use of formaldehyde in this study is motivated by its prevalence in the literature for comparisons to autoignition experiments, such as in Ma et al. [30].

In the two-stage ignition regime, the ignition delay associated with low-temperature ignition can significantly precede the high-temperature ignition, i.e. $\tau_{ign}^{LT} \ll \tau_{ign}^{HT}$. This is shown in Fig. 1c, which shows $0 < \tau_{ign}^{LT}/\tau_{ign}^{HT} < 1$ for a range of mixtures exhibiting two-stage ignition, and that at temperatures greater than approximately 750 K, two-stage ignition is no longer observed and τ_{ign}^{LT} is no longer defined. In particular, for temperatures around 700 K, the low-temperature ignition is seen to significantly precede high-temperature ignition for a wide range of both fuel-lean and fuel-rich mixtures. This is shown quantitatively in Fig. 1d, where at 700 K, τ_{ign}^{LT} is shown to precede τ_{ign}^{HT} for near-stoichiometric mixtures by up to an order of magnitude. Of greater interest, however, is that the low-temperature ignition at 700 K also significantly precedes the single-stage high-temperature ignition at 1000 K. This is in stark contrast with the case of $T_u = 1200$ K, also shown in Fig. 1d, where the high-temperature ignition associated with this temperature precedes the low-temperature ignition of the lower temperatures by an order of magnitude. Figure 1d also shows that for all T_u considered, τ_{ign} decreases with increasing Z for constant T_u. Thus, for a range of both lean and rich mixture compositions, n-dodecane/air chemistry can result in greatly varied ignition behavior, including NTC and two-stage ignition, depending upon initial mixture temperature.

3.2. Physical configuration

The physical configuration considered in this study, shown schematically in Fig. 2, is of a pressurized liquid hydrocarbon delivery conduit which has undergone a localized failure at a distance $L = 0.02$ m from a hot surface. The resulting leakage flow issues in the form of a polydisperse liquid n-dodecane spray from a small orifice of diameter $d_o = 0.18$ mm and impinges upon the surface at a perpendicular nominal angle. Since the leakage flow is small, the conduit pressure remains constant, resulting in a constant spray mass flow rate $\dot{m}_f = 0.05$ g/s, injected droplet speed $V_d = 3.0$ m/s and a nominal spray cone angle $\theta_0 = 15°$. The void space between the pressurized conduit and the hot surface consists initially of quiescent air with a linear temperature profile between the conduit at temperature $T_f = 400$ K and the surface at $T_w > T_f$, and is open to ambient conditions at pressure $p_0 = 1$ atm.

The configuration shown in Fig. 2 was selected to be similar to configurations which have been used in previous studies of head-on quenching and spray-wall interaction [43–46]. The dimensions and spray parameters were selected following the correlations of Lefebvre and Arrowsmith [47] for injection from a plain orifice to ensure the domain size was computationally tracktable and that the parameters chosen were consistent with the configuration considered. In modeling the spray injection, droplet diameters were sampled from a Rosin-Rammler distribution with an injected Sauter mean diameter $D_0 = 100 \mu$m and stretching factor $q = 3.0$, and were injected with a Gaussian spread about the nominal spray cone angle. Physical properties of n-dodecane, namely the liquid density ρ_l, liquid dynamic viscosity μ_l and surface tension σ, at the system pressure and injection temperature are provided in Table 1.

It was shown in Section 3.1 that at atmospheric pressure, n-dodecane/air ignition delay time is a highly non-monotonic function of temperature and mixture fraction, exhibiting two-stage ignition in the NTC regime. The initially linear temperature profile between the conduit and wall results in all temperatures $T_f \leq T \leq T_w$ being accessed within the domain. We thus consider T_w parametrically in this study, with $T_w > T_{HSI}$ to ensure ignition is achieved. Two surface temperatures are considered in this parameter study: 1000 K and 1200 K, as noted in Table 2. In the present configuration where a range of temperatures exists between 400 K and 1000 K, a low-temperature ignition associated with locations in the domain having substantially lower temperatures than T_w may precede the high-temperature ignition associated with locations in the domain having temperatures near T_w. Low and high temperature ignitions depend also on composition, as was shown in Fig. 1d. At $T_w = 1200$ K, however, the high-temperature ignition of the highest temperatures in the domain, namely near T_w, would be expected to occur much more rapidly than any low-temperature ignition across a broad range of mixture compositions. This expected difference in behavior motivates the choices of T_w used in this study.

3.3. Computational setup

Two computational domains were considered, as noted in Table 2, namely a 'full' geometry and a 'quarter' geometry. The full geometry corresponds to a square cuboid of depth L and side length $2.5L$. The wall boundary is prescribed as no-slip and isothermal, with other boundaries prescribed as constant-pressure outlets. The geometric details of the pressurized fuel conduit are neglected and are assumed to lie outside of the computational domain. The fuel spray is injected into the domain from the point $x = L$, $r = 0$. A second-order essentially non-oscillatory (ENO) scheme is applied to the pressure outlets for a depth of five computational cells to eliminate pressure oscillations.

The quarter geometry considers a quarter-section of the full geometry, applying symmetry boundary conditions along the cut planes, with all other boundary conditions identical to the full geometry case. Simulation results for the full and quarter geometries are directly compared at $T_w = 1000$ K in Cases TW1000F and TW1000Q to ensure that the quarter geometry captures all relevant physics. The lower T_w is used for this comparison since it

results in a longer ignition delay time, and thus ensures that the quarter geometry is evaluated across the full range of dynamics considered in the T_w parameter study. The quarter geometry is then used for the T_w parameter study to achieve a reduced computational cost.

The computational mesh is purely hexahedral, with uniform isotropic spacing of $\Delta = 0.217$ mm in the region where the most important mixing and ignition dynamics are expected, $0 < x/L \leq 1/2$. It is then smoothly stretched along the axial direction in the range $1/2 < x/L < 1$ to a maximum spacing of 0.95 mm at $x/L = 1$, with a total mesh size of 6.8 million hexahedral elements for the full geometry and 1.7 million elements for the quarter geometry.

Considering the resolution-limiting case of a fully-premixed and stoichiometric laminar n-dodecane/air flame with an unburned gas temperature corresponding to the highest temperature in the domain prior to ignition $T_u = T_w$, then among all cases in Table 2, the limiting flame thickness is 0.22 mm, such that the present grid resolution results in a thickened flame front being resolved by at least five mesh points. It has been shown in the literature that care must be taken in selecting a thickening sensor for autoignition simulations using LES to achieve accurate predictions of ignition delay [48,49]. A sensitivity analysis of ignition kernel formation to flame thickening was thus conducted, on the basis of which hydroxyl mass fraction was chosen as the flame sensor. The thickening threshold was tuned [48] such that ignition kernels would incur no thickening, thereby ensuring fidelity in the representation of the ignition process, with thickening only becoming active for propagating flame fronts.

Also key to ensuring a high-fidelity representation of the present configuration is the resolution of the thermal boundary layer formed at the hot surface. As has been discussed in the literature [50,51], the wall shear stress in wall-impinging jets is zero at the stagnation point, increases to a maximum at a small radial distance, and then decreases monotonically with radial distance. We performed an inert-flow mesh convergence study to ensure that the near-wall dynamics were well-captured, and found that the present mesh resolution yields a wall grid cell height of $y^+ \leq 2$ at the point of maximum wall shear stress.

As noted in Section 1, for $T_w > T_{L,dyn}$, spray-wall interactions are governed by the impact energy [23], which in the spray-wall interaction model discussed in Section 2.3 is represented by We_n. Estimating We_n by considering Stokes drag along the ballistic spray cone trajectory to obtain the impact velocity, we have

$$We_n = We_0 \left(\cos\theta_0 - 18 \frac{l}{r_\rho Re_0} \right)^2, \tag{5}$$

where $We_0 = \rho_l V_d^2 D_0/\sigma$, $Re_0 = \rho V_d D_0/\mu$, $r_\rho = \rho_l/\rho$ and $l = L/D_0$. Considering that both droplet sizes and trajectories are sampled from statistical distributions, the range of possible impact Weber numbers in the present estimation is $0 < We_n \lesssim 50$. Based on the experimental evidence [15,16], since $(T_w - T_{sat})/(T_L - T_{sat}) > 4$ for all cases considered in this study, impinging droplets are expected to inelastically rebound from the hot surface without break-up, and the model proposed in Section 2.3 is thus applicable.

4. Theoretical analysis of gas-phase fluid dynamical structure

The fluid dynamics of both laminar (e.g. [52,53]) and turbulent (e.g. [50,51]) wall-impinging gaseous jets has been studied in detail. The key difference in the present case is that the gaseous flow is in fact a secondary flow driven by momentum exchange with the injected spray. Considering the parameter values discussed in Section 3.2, we have a nominal droplet Stokes number $St = \rho_l D_0^2 V_d/(18\mu_g L) \sim 1$, and $Re_0 \sim 1$. It is thus assumed that sufficient droplet momentum is transferred to the gas phase to
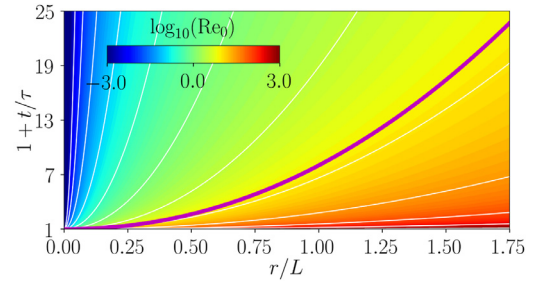

Fig. 3. Non-dimensional temporal evolution of the near-wall gaseous fluid dynamical structure of a turbulent wall-impinging jet based on Eq. (6), with $\delta = 2$, $l = 200$. The isocontour of $Re_0 = 8$, shown in magenta, corresponds to the spray injection conditions of the present study.

warrant consideration of an equivalent jet Reynolds number Re^* as the ratio of injected liquid-phase inertia $\rho_l V_d d_o$ to restorative gas-phase viscosity μ_g, and thus we have $Re^* = Re_0 \delta r_\rho \sim 10,000$, where $\delta = d_o/D_0$. Based on the magnitude of Re^*, the turbulent wall-impinging jet scaling analysis is considered.

It is conceptually useful to divide the flow temporally into an unsteady regime prior to the first spray-wall interaction $0 < t/\tau < 1$, a quasi-steady regime once the core of the wall-impinging jet has been established prior to ignition $1 < t/\tau < t_{ign}/\tau$, and the post-ignition regime $t/\tau > t_{ign}/\tau$, where t_{ign} refers to the ignition delay time observed in the heterogeneous multiphase system and $\tau = L/V_d$ is the characteristic fluid dynamical time scale corresponding to the nominal ballistic flight time of injected droplets. In the quasi-steady regime, shown schematically in Fig. 2, there exists a central axial jet region surrounded by a wall jet [54], at the outer extent of which is a toroidal vortex. Here, we modify the formulation of Poreh et al. [55] and Song and Abraham [56] for the case of liquid spray injection, neglecting the effect of spray-wall interaction on the gaseous flow, to scale the temporal evolution of the wall jet tip r_{tip}, which we define as the location where the maximum radial velocity has reached some fraction of its steady-state value. Re-writing the quasi-steady similarity solution results presented by Poreh et al. [55] in terms of the non-dimensional parameters used in this work, we obtain

$$\frac{r_{tip}}{L} \sim \left(Re_0 \frac{\delta^2}{l} \frac{t}{\tau} \right)^\eta \tag{6}$$

where $\eta \approx 0.5$ was determined empirically [56]. Equation (6) is plotted in Fig. 3 for the values of δ and l considered in the present configuration using a unity constant of proportionality. The isocontour of $Re_0 = 8$ shows the characteristic radial development of the gas-phase fluid dynamical structure near the wall for the boundary conditions considered in this study.

5. Evaluation of the spray-wall interaction model

We consider the experiments of Chiu and Lin [28] due to the similarity of the experimental conditions to those of the present numerical study, as well as their use of a heavy hydrocarbon fuel with physical properties similar to n-dodecane. The experiment involved the impingement of diesel and diesel-water emulsion droplet trains on an angled stainless-steel plate with $T_w > T_L$ at atmospheric pressure. A range of angles of incidence, impingement velocities and droplet diameters were examined.

We consider the case of a train of pure diesel droplets of $D_d = 830 \mu$m traveling at a speed $V_d = 1.42$ m/s impinging on the hot surface at an angle $\theta = 30°$ as measured from the surface at an image acquisition frequency of 350 Hz (case A1 in the reference, $We_n = 12.2$). The experimental imagery from the reference was post-processed to extract droplet outlines and centroids, and are
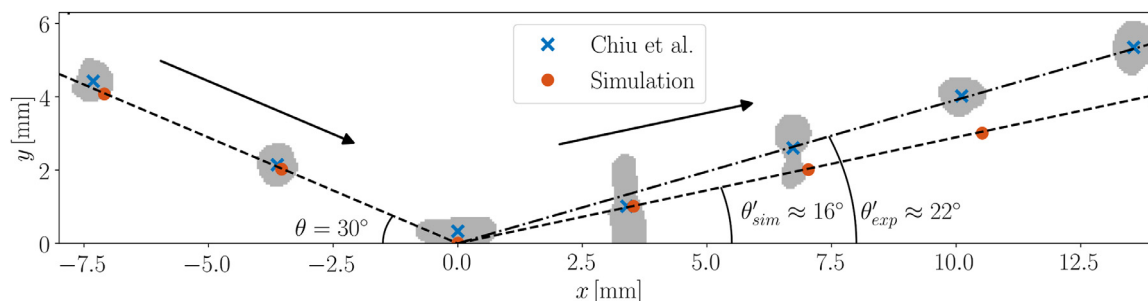
Fig. 4. Evaluation of the spray-wall interaction model using experimental data from Chiu and Lin [28] (case A1, $We_n = 12.2$). Experimental imagery of droplets is shown in grey, and blue crosses show their centroids. Results were shifted horizontally such that the origin coincides with the point of impact. Arrows show the direction of droplet motion before and after impact. Dashed lines show the purely ballistic trajectory, with collision inelasticity from Eq. (4). The dash-dotted line is a least-squares fit to the post-impact droplet centroids passing through the origin. (For interpretation of the references to color in this figure legend, the reader is referred to the web version of this article.)

plotted in Fig. 4. The droplet centroids are seen to follow a trajectory commensurate with that of an inelastic collision, and the shape of the droplet is seen to undergo significant deformation during and after the collision. Applying the same gas and liquid-phase boundary conditions as in the experiment and employing the spray-wall interaction model of Section 2.3 this case was simulated numerically. No reactive behavior was reported in the experiment, and thus the reaction source term in Eq. (1) was neglected. Liquid properties for diesel fuel were used as they were reported in the experiment, shown in Table 1. The droplet trajectory was found to be nearly ballistic and insensitive to mesh resolution. Simulation results for droplet positions are plotted in Fig. 4. Both experimental and numerical results were shifted horizontally such that the origin coincides with the point of impact.

From Fig. 4 it can be seen that the simulation results agree well with the droplet centroid positions throughout the interaction event, with some deviation on the order of one droplet diameter visible after impact. Considering the post-impact trajectories, the experimental angle of inelastic reflection is $\theta'_{\exp} \approx 22°$, whereas that of the simulation is $\theta'_{sim} \approx 16°$. From Eq. (4) and assuming the wall-parallel component of the droplet velocity remains approximately constant, these correspond to $L_{n,exp} \approx 0.30$ and $L_{n,sim} \approx 0.50$, respectively. Deviation of this order is to be expected, since the point-particle method employed cannot fully capture the complex dynamics of the severe droplet deformation during and after impact. Indeed, the level of agreement observed is commensurate with that of the spread in the original data [23] from which Eq. (4) was obtained, as well as the spread in the data of [28] where Eq. (4) was applied to a heavy hydrocarbon fuel and compared to experiments for a range of We_n. Given that the spray-wall interaction model recovers the key physical feature of the interaction with reasonable accuracy, namely that of a reduction in wall-normal momentum, the present implementation is deemed adequate for the ignition study considered in this work.

6. Results and discussion

6.1. Flow structure

We consider first an overview of the simulation results in order to generate a physical understanding of the processes at play. To this end, Fig. 5 shows the development of the fluid dynamical structure and subsequent hot surface ignition of the wall-impinging spray considered for each of the cases outlined in Table 2. Key simulation results are summarized in Table 3, where ignition is defined as the first position in space and time to reach $T = 1500$ K. In Fig. 5, the stoichiometric mixture fraction isosurface is used to show the development of the flow field, and

Table 3
Summary of ignition kernels formed in all cases studied, where ignition is defined as the first position in space and time to reach $T = 1500$ K.

Case	t_{ign}/τ	r_{ign}/L	x_{ign}/L
TW1000F	18.0	1.26	0.06
TW1000Q	16.6	1.31	0.06
TW1200Q	2.2	0.35	0.03

the $T = 1500$ K isosurface is used to show the development of ignition kernels and the propagation of the ensuing flame front.

For all cases, it is seen that a jet-like core is formed by the evaporating injected spray, which arrives at the hot surface at approximately $t/\tau = 1.2$, since droplets are not injected perfectly normal to the wall, nor are they entirely ballistic. Recalling that the system is initially quiescent with a constant temperature gradient away from the hot surface, the mixture fraction field thus develops as a result of spray-gas interaction: the gas-phase temperature field influences the evaporation of the liquid phase which produces gaseous mixture fraction. The fluid motion is driven by the momentum exchange of the injected spray with the gas phase. The interaction of the spray with the wall, as governed by the Leidenfrost effect, discussed in Section 1, results in the inelastic reflection of the impinging droplets. Reflected droplets both disturb the developing mixture fraction field through momentum interactions and continue to evaporate on their outward trajectory, resulting in the streaking structures visible around the outside of the stoichiometric isosurface.

In case TW1200Q, the high wall temperature results in the rapid formation of an ignition kernel near the wall at $x/L = 0.03$, visible at $t/\tau = 2.4$. The kernel propagates along the stoichiometric contour and the system transitions to a quasi-steady fully-burning state, with a partially-premixed flame burning on the stoichiometric contour. The presence of a steady burning flame will be further examined in Section 6.3. The simulation was not continued beyond the establishment of the fully-burning state, since the focus of this study is on the dynamics of ignition and initial flame propagation.

In cases TW1000F and TW1000Q, the system develops quite differently. As expected from the analysis of Section 3.1, the lower wall temperature results in a delayed formation of ignition kernels, and thus allows the flow field to develop the toroidal vortical structure associated with wall-impinging jets discussed in Section 4 more completely. This is seen in Fig. 5 for $3.3 \leq t/\tau \leq 16.9$. Cases TW1000F and TW1000Q form ignition kernels along the stoichiometric contour within 1.4τ of each other temporally, and further from the wall than case TW1200Q, at $x/L = 0.06$. Like in case TW1200Q, these kernels transition to flame fronts which propagate along the stoichiometric contour. However,
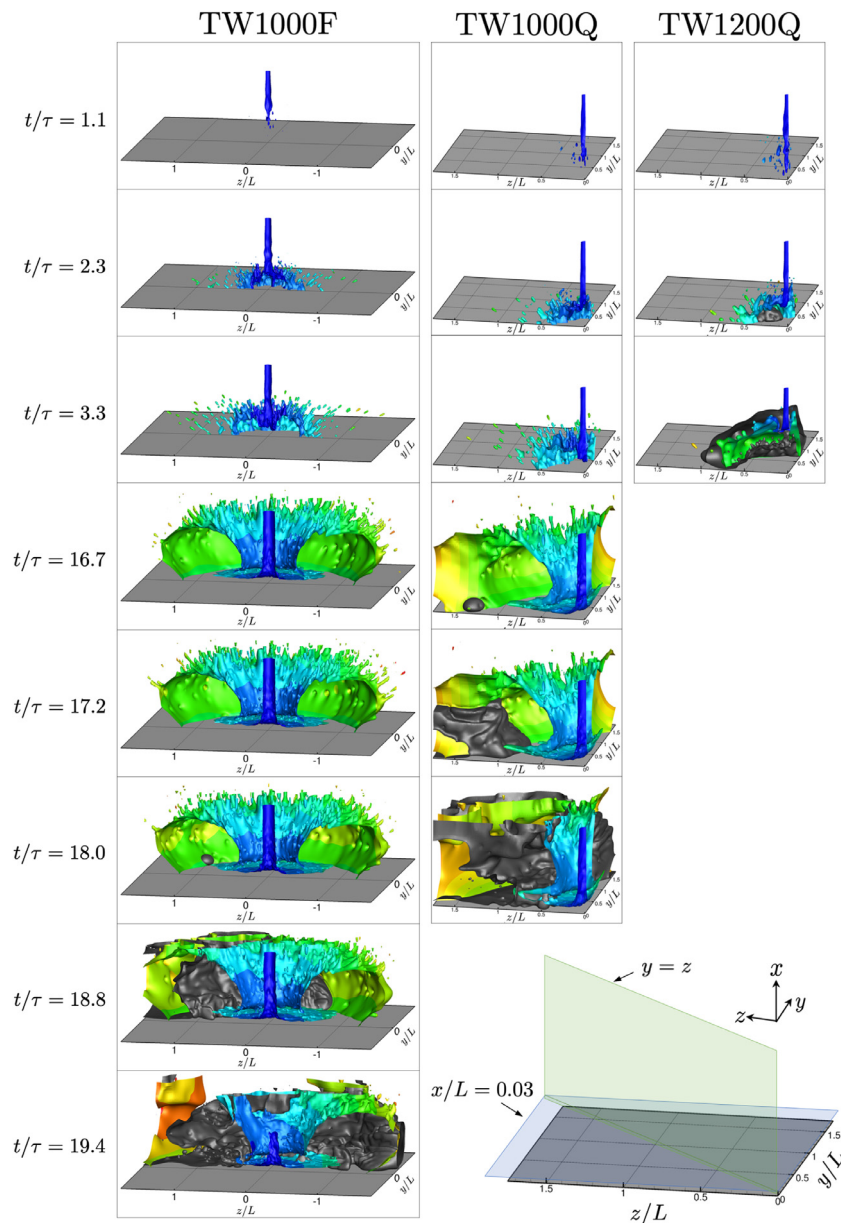
Fig. 5. Temporal evolution of the ignition process for all cases considered. The instantaneous stoichiometric Bilger mixture fraction isosurface $Z = Z_{st}$ is colored by radial distance from the central axis for visual contrast. The temperature isosurface $T = 1500\,\mathrm{K}$ is shown in gray to represent the flame. Results for TW1000F are shown in half of the domain to better illustrate the structure of the fields considered. The bottom right panel shows the two reference planes that will be used in this study to show results: blue shows the $x/L = 0.03$ plane, and green shows the $y = z$ radial plane. (For interpretation of the references to color in this figure legend, the reader is referred to the web version of this article.)

in cases TW1000F and TW1000Q, the changes in the flow field dynamics caused by the propagating flame front are far greater than in case TW1200Q, where instead of transitioning to a steady-burning state, the flame propagates to envelop most of the domain and causes substantial distortion of the stoichiometric isosurface.

6.2. Azimuthally-averaged spatio-temporal analysis

The development of the flow field is next analyzed quantitatively by considering the temporal variation in the Z-field near the wall. Noting the azimuthal symmetry of the boundary conditions about the x-axis, the instantaneous Z-field was azimuthally averaged on a wall-parallel plane at $x/L = 0.03$, such that the development of the Z-field could be expressed as a function of r and time. The Z_{st} contour was then extracted, and is plotted in spatio-temporal coordinates in Fig. 6 for all cases considered. We hy-
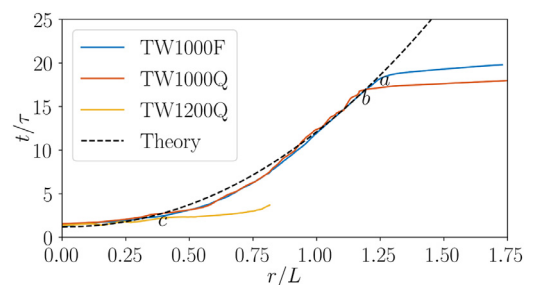

Fig. 6. Spatio-temporal evolution of azimuthally-averaged Z_{st}-isocontour on a wall-parallel plane at $x/L = 0.03$ (see Fig. 5 for orientation). Theoretical results from Eq. (6) consider $\delta = 2$, $l = 200$ and $Re_0 = 8$ with a constant of proportionality of 0.75. Labels a, b and c show the inflection of the Z_{st} profile associated with ignition and subsequent flame propagation for cases TW1000F, TW1000Q and TW1200Q, respectively.

pothesize that the temporal development of the Z_{st} contour near the wall is driven primarily by the formation of the wall jet discussed in Section 4. Thus, assuming a Schmidt number of order one, Eq. (6) was also plotted in Fig. 6 with parameters as discussed in Section 4 and assuming the wall jet would only begin to form after the beginning of spray-wall interaction at $t/\tau = 1.2$.

Considering the simulation results in Fig. 6, the Z_{st} contour is seen to develop from the injection axis at $r = 0$ outwards after the delay of approximately 1.2τ due to the flight time associated with the injected droplet stream. The mixture fraction produced by the evaporation of the incoming droplets is then driven by the secondary flow arising from the droplet drag in a jet-like core toward the stagnation point at $x = 0$, $r = 0$ and then radially outwards by the developing wall jet. In cases TW1000F and TW1000Q, as was shown in Fig. 5, the formation of the wall jet drives the development of a toroidal vortex about the central axis and causes the Z_{st}-isosurface near the wall to move radially outwards over time, following the $r \propto t^{0.5}$ power law of Eq. (6) discussed in Section 4. This remains the case until t_{ign}, labeled a and b in the figure for cases TW1000F and TW1000Q, respectively, when the increase in gaseous temperature associated with ignition and rapid flame propagation results in an inflection in the Z_{st} curves due to an increased rate of droplet vaporization.

It is noteworthy that the result from Eq. (6) is in close agreement with the curves of cases TW1000F and TW1000Q prior to ignition within an order-one constant, here taken as 0.75. This close agreement shows the validity of the turbulent wall jet scaling analysis of Section 4 in describing the near-wall dynamics of the present wall-impinging spray prior to ignition, at which point the dynamics driven by rapid changes in gas-phase temperature and the associated gaseous expansion and increased spray vaporization overwhelm those of the expanding wall jet. The rapid ignition of case TW1200Q, labeled c in Fig. 6, results in a much earlier departure from the scaling law result relative to the lower wall temperature cases.

Prior to ignition, the curves in Fig. 6 for cases TW1000F and TW1000Q are seen to be in close quantitative agreement. Furthermore, the difference in the spatio-temporal localization of their ignition kernels in terms of t_{ign}, r_{ign} and x_{ign}, summarized in Table 3, is 8%, 4% and less than 6%, respectively. The ignition process in the present study is stochastic, as it is driven by different aspects of the stochastically-injected spray field. The close quantitative agreement in the spatio-temporal localization of the ignition kernels and the temporal development of Z_{st} in cases TW1000F and TW1000Q shows that between the full and quarter geometries, the problem is insensitive to the azimuthal extent considered. All ensuing analysis will therefore focus on cases TW1000Q and TW1200Q.

It should be noted that since the analysis of this study will rely on single realizations and that ignition is driven by local thermochemistry, the quantitative results obtained are prone to statistical error owing primarily to the stochastic spray boundary condition considered. Table 3 shows that in cases TW1000F and TW1000Q, $t_{ign} \gg \tau$, indicating that the local thermochemistry leading to the formation of ignition kernels is less prone to statistical error stemming from the effects of a single droplet than case TW1200Q, where $t_{ign} \sim \tau$. This is because a larger sample of injected droplets ultimately lead to ignition in the lower wall temperature cases. The undertaking of sufficient realizations to achieve statistical convergence of all quantitative results would require an inordinate amount of computational resources at the level of fidelity considered here, and is considered outside the scope of this study, which has as its focus the analysis of the physical processes at play.

It is of interest to compare the temporal development of the radial Z profile for the different T_w considered, as is shown in Fig. 7. In both cases TW1000Q and TW1200Q, the highest mixture fractions are seen to occur near the injection axis at $r = 0$. In case

TW1000Q, however, the change in Z with increasing r is seen to be non-monotonic, owing to the enhanced mixing of the temporally-expanding toroidal vortex. Finally, it is seen that although the radial extent of the Z_{st} contour in case TW1200Q is less than that of case TW1000Q, a broader range of rich mixture fractions is accessed in the former.

6.3. Instantaneous flow field analysis

In this section, the development of the flow field is analyzed through its thermo-chemical structure. Figures 8 and 9 show the temporal development of the flow structure for cases TW1000Q and TW1200Q, respectively. In both figures, panel (a) shows instantaneous results of Z, Y_{CH_2O}, Y_{OH} and T/T_w in physical space, at multiple instances in time which are illustrative of the physical processes discussed. Panel (b) of both figures shows global scatter data for temperature in mixture fraction space and panel (c) shows global scatter data for Y_{CH_2O} and Y_{OH} as a function of temperature, both at the same time instances as panel (a).

As discussed in Section 6.2, the mixture fraction field develops in tandem with the formation of the toroidal vortex. In case TW1000Q, the ignition process takes $\mathcal{O}(10\tau)$, and hence once ignition occurs at $t/\tau = 16.6$, the vortical structure is well established. This is clear from the top row of Fig. 8a, and in particular from the structure of the Z_{st}-contour, which shows that the interior of the vortical structure is fuel-rich. The vortical motion gives rise to an inert mixing structure, as seen in Fig. 8b, where points are colored by x/L. By $t/\tau = 14.4$, the figure shows that the mixing structure results in a range of rich and lean mixture conditions to be present near $x/L = 0$ and $T = T_w$. After ignition and during flame propagation, the mixing structure is seen to be significantly disturbed, as expected given the highly dynamic nature of the post-ignition behavior of case TW1000Q, as was shown in Fig. 5. By contrast, case TW1200Q has a much shorter time to ignition, and hence the vortical structure is smaller and less developed than in case TW1000Q. This is clearly visible when comparing the first row of Fig. 9a with that of Fig. 8a. The associated mixing structure is also less developed prior to ignition at $t/\tau = 2.2$, as seen in Fig. 9b, where at $t/\tau = 2.1$ the fuel-rich mixture fractions remain sparsely represented. After ignition and during flame propagation, a steady flamelet-like structure is established, supportive of the observation that case TW1200Q transitions rapidly from ignition to a steady-burning flame. It is noteworthy that in both cases TW1000Q and TW1200Q, the production of gaseous mixture fraction due to evaporation results in the reduction of gas-phase temperatures near the wall about the injection axis such that $T < T_w$, as seen in the third rows of Figs. 8a and 9a.

We consider next the presence of chemical species to obtain further insight into the ignition process. It was shown in Section 3.1 that the low-temperature ignition process results in a rapid increase in Y_{CH_2O}, and that the high-temperature ignition of mixtures at 1000 K is significantly preceded by the low temperature ignition of mixtures near 700 K for a range of mixture fractions. It was further shown that Y_{CH_2O} increases rapidly immediately prior to high-temperature ignition, before being fully consumed. In case TW1000Q, these processes are seen to be at play. In Fig. 8a, Y_{CH_2O} is seen to form and achieve its highest concentration within the fuel-rich toroidal vortex. The presence of Y_{CH_2O} in this region is indeed indicative of low-temperature ignition, as is evidenced by the peak in Y_{CH_2O} around $T/T_w = 0.7$ in Fig. 8c for panels where $5.2 \leq t/\tau \leq 17.0$. The low-temperature ignition, visible already at $t/\tau = 5.2$, significantly precedes the high-temperature ignition at $t/\tau = 16.6$. High-temperature ignition and subsequent flame propagation result in a second peak in Y_{CH_2O} in Fig. 8c near $T/T_w = 1.1$. At $t/\tau = 17.0$, Y_{CH_2O} is seen to be fully consumed only within the high-temperature flame zone, identifi-
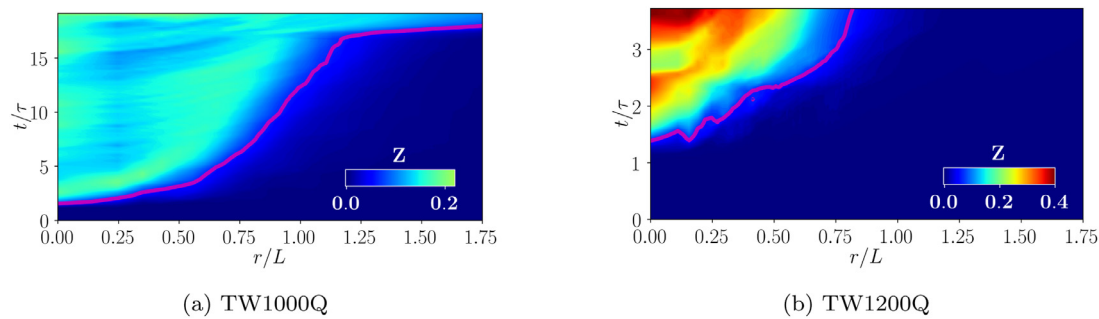
(a) TW1000Q

(b) TW1200Q

Fig. 7. Spatio-temporal evolution of mixture fraction azimuthally-averaged on a wall-parallel plane at $x/L = 0.03$ (see Fig. 5 for orientation). A consistent color scale is used between the two figures. The solid magenta curve shows the evolution of the Z_{st} isocontour.
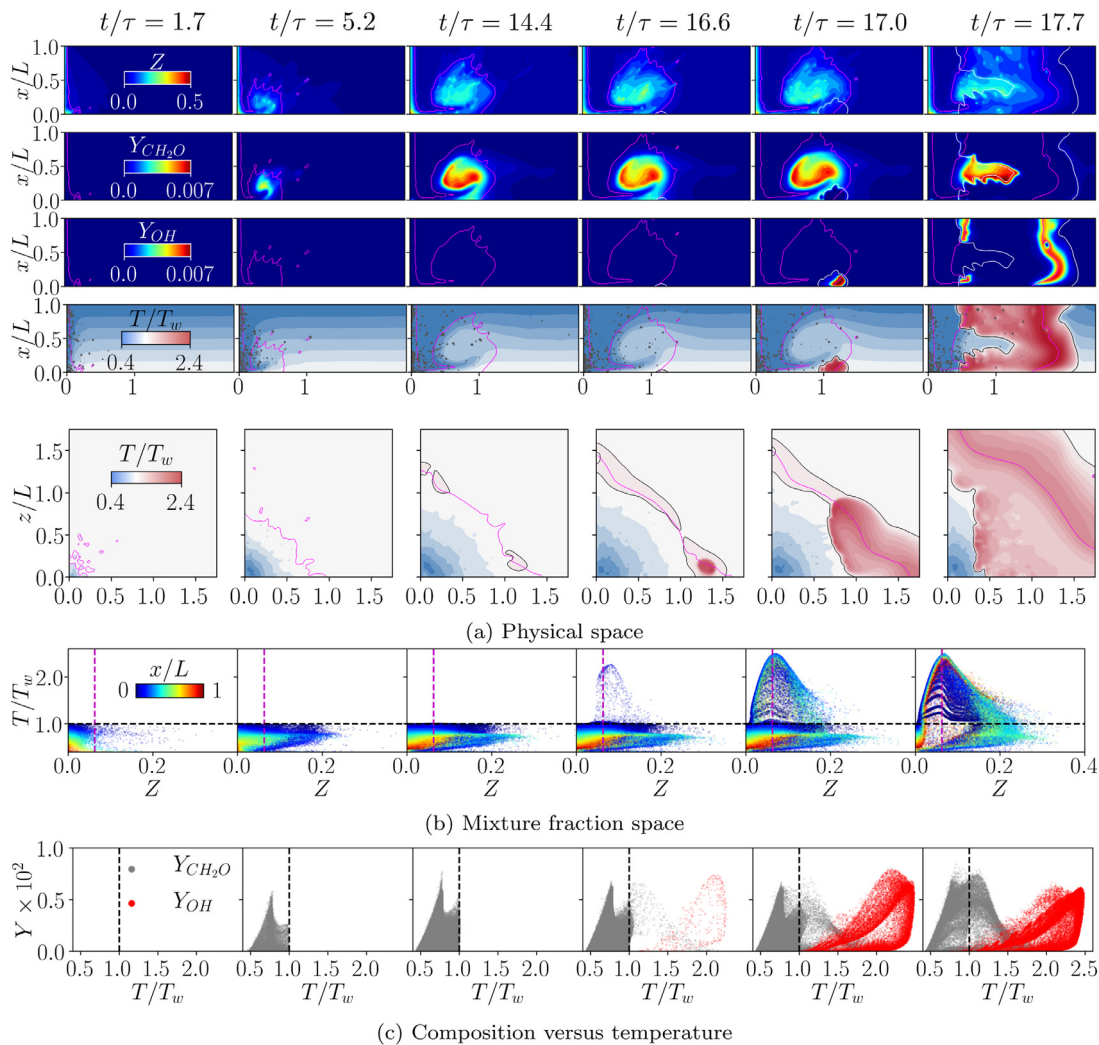

(a) Physical space

(b) Mixture fraction space

(c) Composition versus temperature

Fig. 8. Temporal evolution of the ignition process for case TW1000Q. (a) Instantaneous results for Z, Y_{CH_2O}, Y_{OH} and T/T_w on the wall-perpendicular plane $y = z$, with the fourth row also showing a sampling of fuel droplets in grey, and the bottom row showing T/T_w on the wall-parallel plane $x/L = 0.03$. See Fig. 5 for the orientation of these planes. Magenta lines show isocontours of $Z = Z_{st}$. White and black lines show isocontours of $T = T_w$ in the top three and bottom two rows, respectively. (b) Global scatter data in Z-space colored by x/L. (c) Global scatter data of Y_{CH_2O} and Y_{OH} versus T/T_w, showing low and high-temperature ignition events.

able by the $T/T_w = 1$ contour in Fig. 8a. In Section 3.1, it was also shown that the high-temperature ignition of mixtures at 1200 K significantly precedes the low temperature ignition of any mixture, regardless of temperature or mixture fraction. This is seen for case TW1200Q in Fig. 9c at $t/\tau = 2.1$, with high-temperature ignition occurring near the wall after the formation of Y_{CH_2O} near $T/T_w = 1.0$. Once the system transitions to a steady-burning flame,

Y_{CH_2O} is produced in the fuel-rich region near the stagnation point where $T/T_w \approx 1.0$, as seen from Fig. 9a, 9c.

Gas-phase temperature and the presence of the hydroxyl radical are used to study the formation and propagation of high-temperature ignition kernels. Considering the third and fourth rows of Figs. 8a and 9a, ignition kernels form near the wall and propagate along the stoichiometric contour in both cases, with
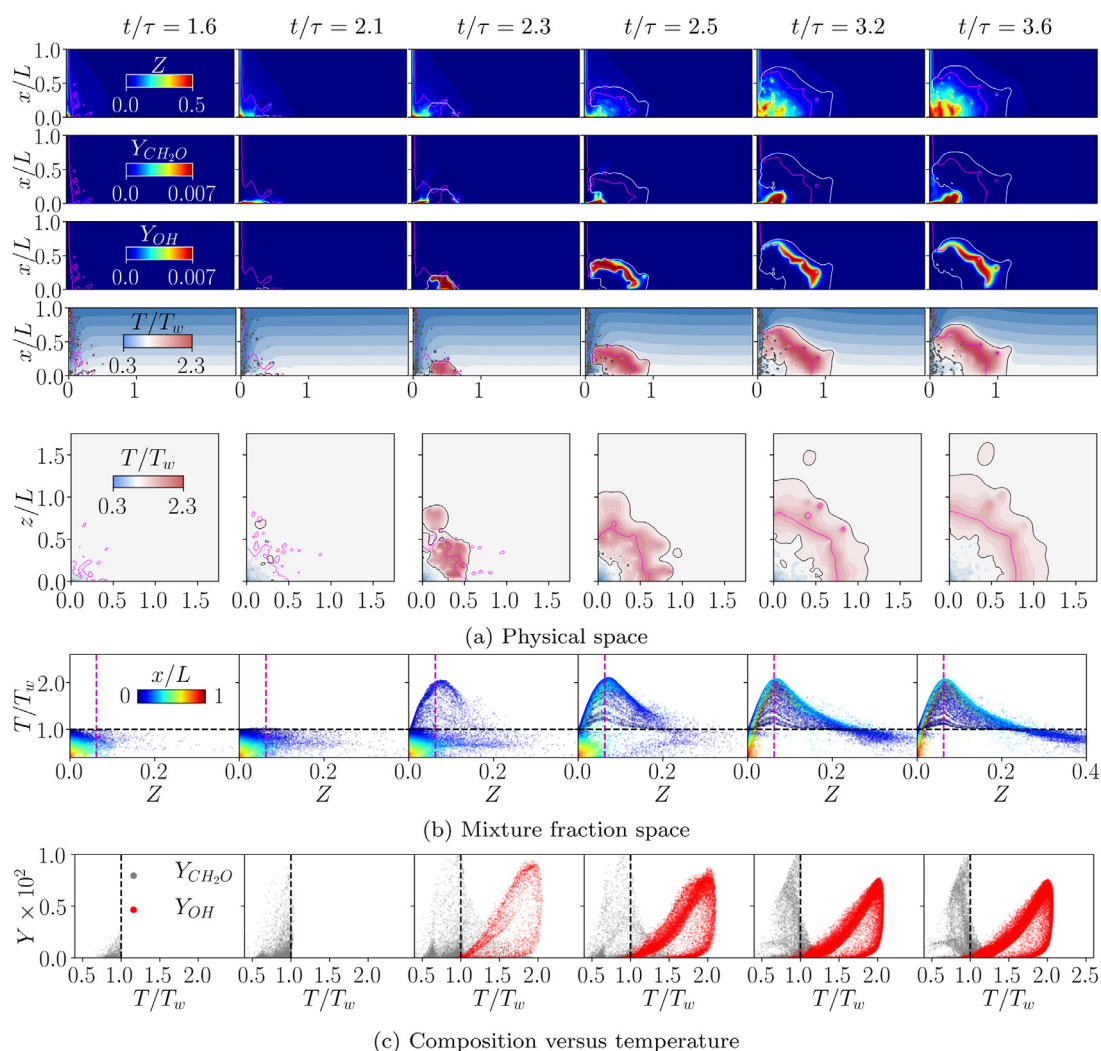
Fig. 9. Temporal evolution of the ignition process for case TW1200Q. (a) Instantaneous results for Z, Y_{CH_2O}, Y_{OH} and T/T_w on the wall-perpendicular plane $y = z$, with the fourth row also showing a sampling of fuel droplets in grey, and the bottom row showing T/T_w on the wall-parallel plane $x/L = 0.03$. See Fig. 5 for the orientation of these planes. Magenta lines show isocontours of $Z = Z_{st}$. White and black lines show isocontours of $T = T_w$ in the top three and bottom two rows, respectively. (b) Global scatter data in Z-space colored by x/L. (c) Global scatter data of Y_{CH_2O} and Y_{OH} versus T/T_w, showing the dominance of high-temperature ignition chemistry.

temperatures in ignited regions approaching T_{ad} for a stoichiometric mixture at the respective T_w. The presence of the hydroxyl radical is well-established as an indicator of high-temperature chemistry [30], with OH being produced as CH$_2$O is consumed during high-temperature ignition. Comparing the second and third rows of Fig. 8a for Y_{CH_2O} and Y_{OH}, respectively, then as was noted above, this effect is most clearly visible at $t/\tau = 17.0$, where the presence of OH corresponds directly to the region where CH$_2$O is fully consumed. In case TW1200Q, a clearly-defined flame front can be identified from Y_{OH} after the establishment of the steady flame. Comparing the mixture fraction and Y_{OH} fields shows that the flame is indeed burning in a partially-premixed regime along the stoichiometric contour, which corresponds to the outer extent of the toroidal vortical structure. In case TW1000Q, the flame front is initially less well defined due to the strong dynamics associated with gaseous expansion during the ignition process. Nevertheless, at $t/\tau = 17.7$ a flame can be identified from the Y_{OH} field on both the inner and outer extent of the vortical structure.

6.4. Volume-averaged analysis

The processes leading to ignition and the subsequent flame propagation are considered in terms of mass-weighted volume-averaged quantities in Fig. 10, where the notation $< \phi > = \frac{1}{\rho} \int \rho \phi dV$ is used for a flow field quantity ϕ averaged over the computational domain. We note that the analysis of $< \phi >$ allows for the quantitative comparison of cases TW1000Q and TW1200Q, since the same domain was used, but that the absolute values obtained depend upon the computational domain considered. Using the maximum temperature in the domain T_{max} as a marker for ignition, a time delay between the points of abrupt changes in T_{max} and $< T >$, labeled a and b in the figure, is seen for both cases TW1000Q and TW1200Q. This delay corresponds to the time between the formation of an ignition kernel and its propagation through the domain causing an increase in the average temperature. The increase in $< T >$ in case TW1200Q is much smaller than in case TW1000Q due to the volumetric compactness of the steady burning flame which is established after ignition relative to the extent of flame propagation which occurs in case TW1000Q.

The evolution of fuel in the domain through evaporation is also shown in Fig. 10. In case TW1000Q, the constant rate of fuel injection coupled with interaction of the spray with the gas phase results in mass transfer through spray evaporation and a correspondingly near-linear increase in $< Z >$ until ignition. After ignition and the onset of flame propagation at b, $< Z >$ increases rapidly since the elevated average temperature in the domain results in more
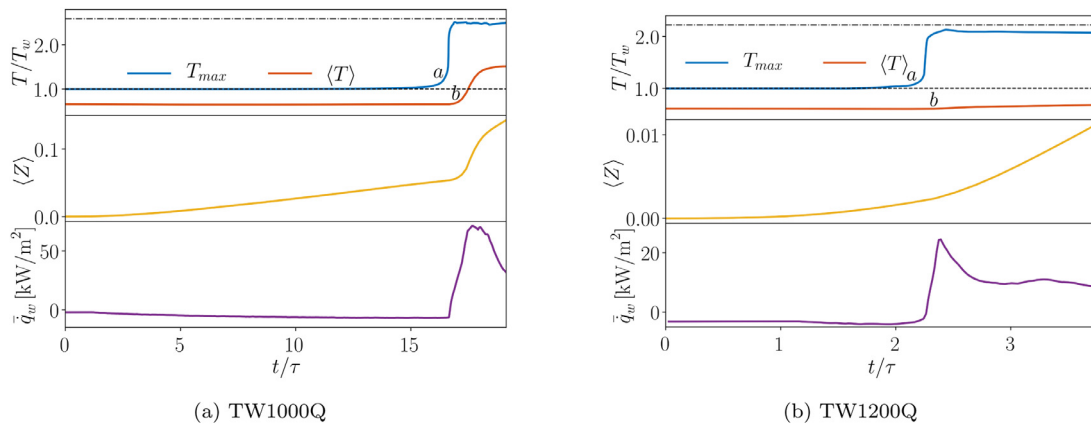
Fig. 10. Temporal evolution of volume-averaged quantities. The dashed line shows T_w and the dash-dotted line the adiabatic flame temperature T_{ad} for a stoichiometric mixture at T_w. $T_{ad} = 2588$ K for case TW1000Q, and $T_{ad} = 2667$ K for case TW1200Q. The labels a and b show the formation of the first ignition kernel and the onset of significant heat release in the domain, respectively.
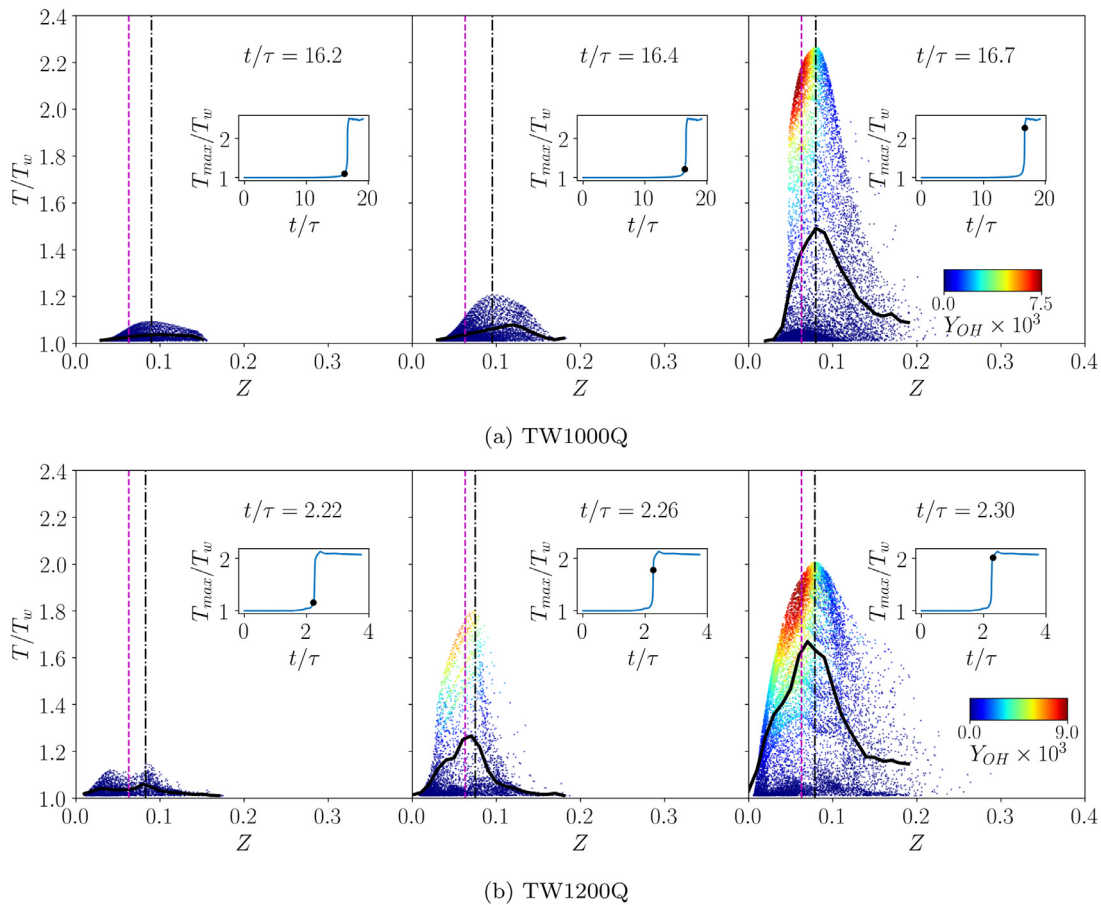

Fig. 11. Temporal evolution of ignition kernels in Z-space. Solid black lines represent T/T_w conditioned on Z, dashed lines show $Z = Z_{st}$ and dash-dotted lines represent $Z|_{T=\max(T)}$ at the time step considered. The inset figures show the progress of ignition through the global maximum temperature, with the black circle on the line denoting the time considered in the panel.

rapid evaporation of droplets. In case TW1200Q, due to the short ignition delay and associated small rise in $<T>$, the same effects are present but less pronounced. $<Z>$ is seen to increase more rapidly after b, but the values remain an order of magnitude smaller than in case TW1000Q, even once the steady burning regime is established.

A key effect of varying T_w is demonstrated in considering the average wall heat flux $\bar{\dot{q}}_w = \frac{1}{A}\int \dot{q}_w dA$ of cases TW1000Q and

TW1200Q, where $\dot{q}_w$ is the local wall heat flux and $A = 1.5625L^2$ is the wall surface area for the quarter geometry. When hot surface ignition occurs, the longer ignition delay time of case TW1000Q due to its reduced T_w relative to case TW1200Q results in a higher value of $<Z>$. This ultimately leads to a greater rise in $<T>$ due to flame propagation throughout a larger portion of the domain, and consequently greater $\bar{\dot{q}}_w$. Indeed, the maximum $\bar{\dot{q}}_w$ during the ignition of case TW1000Q is 2.9 times that of TW1200Q. Thus, we

see that the hot surface ignition of the lower wall temperature case in fact results in a greater maximum heat flux than the higher temperature case.

6.5. Kernel analysis

The formation and propagation of the ignition kernels shown in Figs. 5, 8 and 9 is analyzed in this section in composition space. Here again, ignition is defined as a local temperature rise resulting in $T > 1500$ K. In Fig. 11, global scatter data in composition space is considered at instances illustrative of the kernel formation process. To focus on the ignition process, only points where $T > T_w$ are plotted. Inset plots are included to localize each panel in terms of progress of the global ignition process.

In both cases TW1000Q and TW1200Q, it is clear that the ignition begins at a fuel-rich composition, and moves toward the stoichiometric contour over time, with a large concentration of OH present as the kernel nears T_{ad} and the fully-burning state. The occurrence of ignition initially at fuel-rich compositions is in agreement with the analysis of Section 3.1, where in Fig. 1d it was shown that for equal temperatures, τ_{ign}^{HT} is lowest for $Z > Z_{st}$. The increase in Y_{OH} near T_{ad} is in agreement with the analysis of Fig. 8c and Fig. 9c, where Y_{OH} was used as an indicator of high-temperature ignition. Comparing cases TW1000Q and TW1200Q, it is clear that kernel formation is much quicker in case TW1200Q, and occurs at mixture fractions nearer to Z_{st}. The conditional data show that the initial temperature rise is highly localized, such that the conditional temperature profile for points where $T > T_w$ is largely unaffected before the final panel, at which point the ignition has spread sufficiently in the kernel neighborhood to manifest as a rise in the conditional temperature profile.

7. Conclusions

An impinging fuel spray was analyzed under conditions of hot surface ignition using LES and finite-rate chemistry. Analysis of a low-dimensional model configuration identified wall temperature as a key parameter in determining the ignition dynamics, and it was thus studied parametrically. The wall temperatures considered, namely 1000 K and 1200 K, sufficiently exceeded the fuel Leidenfrost temperature such that spray-wall interaction was modeled as the inelastic rebounding of impinging droplets.

The significantly longer ignition delay of the lower wall temperature case resulted in a more dynamic ignition and flame propagation process than that of the higher wall temperature case. With liquid fuel introduced into the domain at a constant rate, the longer ignition delay resulted in a greater total amount of fuel available for combustion upon ignition. Furthermore, the longer ignition delay allowed the establishment and development of a fuel-rich toroidal vortex about the injection axis, which was shown to promote mixing by entrainment of surrounding air. The rapid ignition of the high-temperature wall case resulted in the establishment of a steady-burning partially premixed flame on the outside of the toroidal vortex. Relative to the lower wall temperature case, the vortical structure was less developed and the extent of flame propagation more volumetrically compact. The lower wall temperature case ultimately resulted in a maximum area-average wall heat flux during ignition nearly three times greater than that of the higher wall temperature.

Despite the wall temperature significantly exceeding the limits of the NTC region, a two-stage ignition process was observed for the lower wall temperature case. As was predicted from analysis of the low-dimensional model, the low-temperature first-stage ignition of mixtures in the NTC region significantly preceded the high-temperature single-stage ignition of mixtures at the wall temperature of 1000 K. The low-temperature ignition occurred within

the fuel-rich vortex, identified by formaldehyde mass fraction. This was then followed by the formation of a high-temperature ignition kernel near the wall at the outer edge of the vortex, which subsequently propagated along the stoichiometric isocontour throughout the domain. As further predicted from analysis of the low-dimensional model, the higher wall temperature case of 1200 K exhibited only a high-temperature ignition near the wall, with the single-stage ignition delay of mixtures at the wall temperature significantly preceding the low-temperature first-stage ignition of all mixtures in the NTC region.

This study provides insight on the complex multiphase phenomena that govern the hot surface ignition of impinging sprays. In particular, conditions were considered where the surface temperature exceeds the Leidenfrost temperature. The importance of low-temperature chemistry and the presence of two-stage ignition phenomena was demonstrated for wall temperatures significantly exceeding the limits of the NTC region.

A practical consideration which arises from this study is that in the analysis of pressurized fuel conduits near hot surfaces, a reduction in surface temperature may not always result in improved outcomes in the event of a leakage. Indeed, this study has shown that in the case of an impinging fuel spray, a surface temperature only mildly exceeding the hot surface ignition limit can result in a more damaging ignition event in terms of transient wall heat flux than a surface temperature far exceeding the ignition limit. This behavior demands of system designers the careful consideration of fuel chemistry, spray-wall interaction and gas-phase secondary flows in addition to surface temperature.

Future work requires the consideration of effects of the impingement angle, fuel mass flow rate and initially non-quiescent domains on the development of mixing structures and subsequent ignition. Transient experimental data for hot surface ignition of liquid sprays at atmospheric conditions is needed to validate simulations and support the development of higher fidelity physical models. In particular, broad parametric studies of geometric configuration, as well as spray and gaseous boundary conditions are needed to promote a deeper understanding of the highly-coupled processes at play.

Declaration of Competing Interest

The authors declare that they have no known competing financial interests or personal relationships that could have appeared to influence the work reported in this paper.

Acknowledgments

References

[1] C.K. Law, On the stagnation-point ignition of a premixed combustible, Int. J. Heat Mass Transf. 21 (11) (1978) 1363–1368, doi:10.1016/0017-9310(78)90199-0.

[2] N.M. Laurendeau, Thermal ignition of methane-air mixtures by hot surfaces: a critical examination, Combust. Flame 46 (1982) 29–49.

[3] P.A. Boettcher, S.K. Menon, B.L. Ventura, G. Blanquart, J.E. Shepherd, Cyclic flame propagation in premixed combustion, J Fluid Mech 735 (2013) 176–202, doi:10.1017/jfm.2013.495.

[4] L.R. Boeck, J. Melguizo-Gavilanes, J.E. Shepherd, Hot surface ignition dynamics in premixed hydrogenair near the lean flammability limit, Combust. Flame 210 (2019) 467–478, doi:10.1016/j.combustflame.2019.09.002.

[5] G. Desoutter, B. Cuenot, C. Habchi, T. Poinsot, Interaction of a premixed flame with a liquid fuel film on a wall, Proc. Combust. Inst. 30 (1) (2005) 259–266, doi:10.1016/j.proci.2004.07.043.

[6] M. Tao, H. Ge, B. VanDerWege, P. Zhao, Fuel wall film effects on premixed flame propagation, quenching and emission, Int. J. Engine Res. 21 (6) (2020) 1055–1066, doi:10.1177/1468087418799565.

[7] G. Kats, J.B. Greenberg, Stagnation-point spray flame ignition by an isothermal surface, J. Eng. Math. 110 (1) (2018) 181–194, doi:10.1007/s10665-017-9947-1.

[8] G. Kats, J.B. Greenberg, Stagnation-point polydisperse spray flame ignition, Combust. Theor. Model. 23 (5) (2019) 771–797, doi:10.1080/13647830.2019.1589580.

[9] J.D. Colwell, A. Reza, Hot surface ignition of automotive and aviation fluids, Fire Tech. 41 (2) (2005) 105–123.

[10] S. Davis, D. Chavez, H. Kytomaa, Hot surface ignition of flammable and combustible liquids, SAE Paper 2006-01-1014 (2006). 10.4271/2006-01-1014

[11] A. Johnson, A. Roth, N. Moussa, Hot Surface Ignition Tests of Aircraft Fluids, Technical Report, Air Force Wright Aeronautical Laboratory, 1988.

[12] Y.L. Li, Y.H. Wang, S.X. Lu, Ignition of the leaked diesel on a heated horizontal surface, Fire Saf. J. 45 (1) (2010) 58–68, doi:10.1016/j.firesaf.2009.10.001.

[13] M.S. Ulcay, L. Dillard, J.P. Gore, Emperical modeling of minimum hot surface ignition temperature for aviation fluids, AIAA Paper 2019–4458 (2019).

[14] B. Chen, L. Feng, Y. Wang, T. Ma, H. Liu, C. Geng, M. Yao, Spray and flame characteristics of wall-impinging diesel fuel spray at different wall temperatures and ambient pressures in a constant volume combustion vessel, Fuel 235 (2019) 416–425, doi:10.1016/j.fuel.2018.07.154.

[15] V. Bertola, An impact regime map for water drops impacting on heated surfaces, Int. J. Heat Mass Transf. 85 (2015) 430–437, doi:10.1016/j.ijheatmasstransfer.2015.01.084.

[16] H.J. Staat, T. Tran, B. Geerdink, G. Riboux, C. Sun, J.M. Gordillo, D. Lohse, Phase diagram for droplet impact on superheated surfaces, J. Fluid Mech. 779 (2015) 1–12, doi:10.1017/jfm.2015.465.

[17] X. Li, D. Xiao, S.E. Parrish, R.O. Grover, D.L. Hung, M. Xu, Dynamics of spray impingement wall film under cold start conditions, Int. J. Engine Res. 21 (2) (2020) 319–329, doi:10.1177/1468087419859682.

[18] R.O. Grover, T.D. Fansler, A. Lippert, M.C. Drake, D.N. Assanis, A numerical-experimental assessment of wall impingement models for spark-ignition direct-injection engines, Int. J. Engine Res. (2019) 1–21, doi:10.1177/1468087419863966.

[19] Y. Kobashi, Y. Zama, T. Kuboyama, Modeling wall film formation and vaporization of a gasoline surrogate fuel, Int. J. Heat Mass Transf. 147 (2020) 119035, doi:10.1016/j.ijheatmasstransfer.2019.119035.

[20] A. Chausalkar, C.B.M. Kweon, S.C. Kong, J.B. Michael, Leidenfrost behavior in drop-wall impacts at combustor-relevant ambient pressures, Int. J. Heat Mass Transf. 153 (2020) 119571, doi:10.1016/j.ijheatmasstransfer.2020.119571.

[21] C. Bai, A.D. Gosman, Development of methodology for spray impingement simulation, SAE Technical Paper 950283(1995).

[22] D. Quéré, Leidenfrost dynamics, Annu. Rev. Fluid Mech. 45 (1) (2013) 197–215, doi:10.1146/annurev-fluid-011212-140709.

[23] A. Karl, A. Frohn, Experimental investigation of interaction processes between droplets and hot walls, Phys. Fluids 12 (4) (2000) 785–796, doi:10.1063/1.870335.

[24] M. Shirota, M.A. Van Limbeek, C. Sun, A. Prosperetti, D. Lohse, Dynamic leidenfrost effect: relevant time and length scales, Phys. Rev. Lett. 116 (6) (2016) 1–5, doi:10.1103/PhysRevLett.116.064501.

[25] R. Miller, K. Harstad, J. Bellan, Evaluation of equilibrium and non-equilibrium evaporation models for many-droplet gas-liquid flow simulations, Int. J. Multiphase Flow 24 (6) (1998) 1025–1055, doi:10.1016/S0301-9322(98)00028-7.

[26] W. Ranz, W. Marshall, Evaporation from drops, part I, Chem. Eng. Prog. 48 (3) (1952) 141–146.

[27] L. Wachters, N. Westerling, The heat transfer from a hot wall to impinging mist droplets in the spheroidal state, Chem. Eng. Sci. 21 (12) (1966) 1231–1238, doi:10.1016/0009-2509(66)85042-X.

[28] S.L. Chiu, T.H. Lin, Experiment on the dynamics of a compound drop impinging on a hot surface, Phys. Fluids 17 (12) (2005) 1–9, doi:10.1063/1.2139101.

[29] M. Gradeck, N. Seiler, P. Ruyer, D. Maillet, Heat transfer for leidenfrost drops bouncing onto a hot surface, Exp. Therm Fluid Sci. 47 (2013) 14–25, doi:10.1016/j.expthermflusci.2012.10.023.

[30] P.C. Ma, H. Wu, T. Jaravel, L. Bravo, M. Ihme, Large-eddy simulations of transcritical injection and auto-ignition using diffuse-interface method and finite-rate chemistry, Proc. Combust. Inst. 37 (3) (2019) 3303–3310, doi:10.1016/j.proci.2018.05.063.

[31] T. Yao, Y. Pei, B.-J. Zhong, S. Som, T. Lu, K.H. Luo, A compact skeletal mechanism for n-dodecane with optimized semi-global low-temperature chemistry for diesel engine simulations, Fuel 191 (2017) 339–349, doi:10.1016/J.FUEL.2016.11.083.

[32] G. Bikas, N. Peters, Kinetic modelling of n-decane combustion and autoignition, Combust. Flame (2001), doi:10.1016/S0010-2180(01)00254-1.

[33] P.C. Ma, H. Wu, J.W. Labahn, T. Jaravel, M. Ihme, Analysis of transient blow-out dynamics in a swirl-stabilized combustor using large-eddy simulations, Proc. Combust. Inst. 37 (4) (2019) 5073–5082, doi:10.1016/J.PROCI.2018.06.066.

[34] D. Mohaddes, W. Xie, M. Ihme, Analysis of low-temperature chemistry in a turbulent swirling spray flame near lean blow-out, Proc. Combust. Inst. 38 (2021). In press

[35] Q. Douasbin, M. Ihme, C. Arndt, Pareto-efficient combustion framework for predicting transient ignition dynamics in turbulent flames: application to a pulsed jet-in-hot-coflow flame, Combust. Flame (2020), doi:10.1016/j.combustflame.2020.09.031.

[36] P.C. Ma, Y. Lv, M. Ihme, An entropy-stable hybrid scheme for simulations of transcritical real-fluid flows, J. Comput. Phys. 340 (2017) 330–357, doi:10.1016/j.jcp.2017.03.022.

[37] H. Wu, P.C. Ma, M. Ihme, Efficient time-stepping techniques for simulating turbulent reactive flows with stiff chemistry, Comput. Phys. Commun. 243 (2019) 81–96, doi:10.1016/J.CPC.2019.04.016.

[38] A.W. Vreman, An eddy-viscosity subgrid-scale model for turbulent shear flow: algebraic theory and applications, Phys. Fluids 16 (10) (2004) 3670–3681, doi:10.1063/1.1785131.

[39] J.P. Légier, T. Poinsot, B. Varoquié, F. Lacas, D. Veynante, Large Eddy Simulation of a Non-Premixed Turbulent Burner Using a Dynamically Thickened Flame Model, Proceedings of the IUTAM Symposium on Turbulent Mixing and Combustion, Kluwer Academic Publishers (2002), pp. 315–326, doi:10.1007/978-94-017-1998-8_27.

[40] D.G. Goodwin, H.K. Moffat, R.L. Speth, Cantera: An object-oriented software toolkit for chemical kinetics, thermodynamics, and transport processes, 2017. 10.5281/zenodo.170264

[41] R. Bilger, S. Stårner, R. Kee, On reduced mechanisms for methane-air combustion in nonpremixed flames, Combust. Flame 80 (2) (1990) 135–149, doi:10.1016/0010-2180(90)90122-8.

[42] J. Zádor, C.A. Taatjes, R.X. Fernandes, Kinetics of elementary reactions in low-temperature autoignition chemistry, Prog. Energy Combust. Sci. 37 (4) (2011) 371–421, doi:10.1016/j.pecs.2010.06.006.

[43] U. Meingast, M. Staudt, L. Reichelt, U. Renz, F.A. Sommerhoff, Analysis of spray/wall interaction under diesel engine conditions, SAE Technical Papers (724) (2000), doi:10.4271/2000-01-0272.

[44] B. Yang, J. Ghandhi, Measurement of diesel spray impingement and fuel film characteristics using refractive index matching method, SAE Technical Papers 2007 (724) (2007), doi:10.4271/2007-01-0485.

[45] J. Gao, S. Moon, Y. Zhang, K. Nishida, Y. Matsumoto, Flame structure of wall-impinging diesel fuel sprays injected by group-hole nozzles, Combust. Flame 156 (6) (2009) 1263–1277, doi:10.1016/J.COMBUSTFLAME.2009.01.014.

[46] A. Wehrfritz, H. Wang, E.R. Hawkes, Y. Gao, T. Lu, Wall-impinging laminar premixed n-dodecane flames under autoignitive conditions, Proc. Combust. Inst. 37 (2) (2019) 1647–1654, doi:10.1016/J.PROCI.2018.06.118.

[47] A. Lefebvre, A. Arrowsmith, Atomization and Sprays, CRC Press, 2017, doi:10.1016/0009-2509(90)87140-N.

[48] A. Misdariis, Schemas cinetiques reduits et couplage thermique pour les simulations aux grandes echelles du cliquetis dans les moteurs a piston, Institut National Polytechnique de Toulouse, 2015 Ph.D. thesis.

[49] Q. Malé, G. Staffelbach, O. Vermorel, A. Misdariis, F. Ravet, T. Poinsot, Large eddy simulation of pre-chamber ignition in an internal combustion engine, Flow, Turbul. Combust. 103 (2) (2019) 465–483, doi:10.1007/s10494-019-00026-y.

[50] T. Dairay, V. Fortuné, E. Lamballais, L.E. Brizzi, Direct numerical simulation of a turbulent jet impinging on a heated wall, J. Fluid Mech. 764 (2015) 362–394, doi:10.1017/jfm.2014.715.

[51] M. Hadžiabdić, K. Hanjalić, Vortical structures and heat transfer in a round impinging jet, J. Fluid Mech. 596 (January 2008) (2008) 221–260, doi:10.1017/S002211200700955X.

[52] H. Schlichting, Boundary-Layer Theory, 8, Springer-Verlag, 2000.

[53] R. Kee, M. Coltrin, P. Glarborg, Chemically Reacting Flow: Theory & Practice, John Wiley & Sons, Inc., 2003.

[54] M.B. Glauert, The wall jet, J. Fluid Mech. 1 (06) (1956) 625, doi:10.1017/s002211205600041x.

[55] M. Poreh, Y.G. Tsuei, J.E. Cermak, Investigation of a turbulent radial wall jet, J. Appl. Mech. 34 (2) (1967) 457–463, doi:10.1115/1.3607705.

[56] L. Song, J. Abraham, Entrainment characteristics of transient turbulent round, radial and wall-impinging jets: theoretical deductions, J. Fluids Eng. Trans. ASME 125 (4) (2003) 605–612, doi:10.1115/1.1593707.

[57] NIST Chemistry WebBook, P. Linstrom, W. Mallard (Eds.), National Institute of Standards and Technology, 2020.

[58] A.A. Mills, J.D. Fry, Rate of evaporation of hydrocarbons from a hot surface: nukiyama and leidenfrost temperatures, Eur. J. Phys. 3 (3) (1982) 152–154, doi:10.1088/0143-0807/3/3/005.

[59] National Center for Biotechnology Information, PubChem Compound Summary for CID 8182, Dodecane, 2020.

[60] J. Bacha, J. Freel, A. Gibbs, L. Gibbs, G. Hemighaus, K. Hoekman, J. Horn, A. Gibbs, M. Ingham, L. Jossens, D. Kohler, D. Lesnini, J. McGeehan, M. Nikanjam, E. Olsen, R. Organ, B. Scott, M. Sztenderowicz, A. Tiedemann, C. Walker, J. Lind, J. Jones, D. Scott, J. Mills, Diesel Fuels Technical Review, Technical Report, Chevron Corporation, 2007.

[61] T.Y. Xiong, M.C. Yuen, Evaporation of a liquid droplet on a hot plate, Int. J. Heat Mass Transf. 34 (7) (1991) 1881–1894, doi:10.1016/0017-9310(91)90162-8.